Journal of
Materials Chemistry B

PAPER

Cite this: J. Mater. Chem. B, 2016, 4, 1331

A layered drug nanovehicle toward targeted cancer imaging and therapy†

Shanyue Guan,[a] Ruizheng Liang,*[a] Chunyang Li,[a] Dan Yan,*[b] Min Wei,*[a] David G. Evans[a] and Xue Duan[a]

Received 1st December 2015,
Accepted 19th January 2016

DOI: 10.1039/c5tb02521d

www.rsc.org/MaterialsB

A layered drug nanovehicle was fabricated *via* the co-intercalation of doxorubicin (DOX) and folic acid (FA) into the gallery of layered double hydroxides (LDHs). This supermolecular nanovehicle (denoted as DOX–FA/LDH) demonstrates excellent fluorescence imaging and targeted therapy toward cancer cells. The nanovehicle shows a uniform platelet morphology with an average diameter of ~171 nm. The unique host–guest interactions lead to a high dispersion of DOX, and *in vitro* tests reveal a legible and strong fluorescence imaging for the DOX–FA/LDH sample. In addition, the DOX–FA/LDH material produces a high anticancer activity toward HepG2 cells but rather low cytotoxicity to the normal cells (L02 cells), as a result of the overexpression of FA towards cancer cells. This work provides a facile approach for the design and preparation of a drug nanovehicle with significantly enhanced biocompatibility, diagnosis and targeted therapy, which can be potentially applied in medical imaging and chemotherapy.

Introduction

Over the decades, as one of the most important therapy methods, chemotherapy has been extensively applied in cancer treatment, owing to its high efficiency and convenience compared with other treatment approaches.[1,2] However, conventional chemotherapeutic agents normally show the following disadvantages: (a) non-specific recognition, (b) poor biocompatibility and solubility, and (c) inefficient cellular internalization.[3,4] These disadvantages often lead to the non-specific uptake by the normal cells and cause obvious side effects.[5–7] In order to resolve the issues mentioned above, the incorporation of chemotherapeutic agents within a suitable nanocarrier is a preferred alternative. To date, multifunctional nanocarriers have attracted considerable attention as a platform to deliver and release drugs. For instance, Fe_3O_4 nanoparticles (NPs),[8,9] SiO_2 NPs,[10,11] Au NPs,[12–16] block polymers[17–20] and micelles[21–24] have been widely studied as drug carriers for cancer therapy. However, they generally suffer from complicated preparation processes, low efficiency of uptake or structure uncontrollability. As a result, the combination of diagnosis and targeting therapy into one system with facile preparation and superior biocompatibility remains a challenging goal.[25,26]

Layered double hydroxides (LDHs) are a class of inorganic layered materials generally expressed as $[M^{2+}_{1-x}M^{3+}_{x}(OH)_2](A^{n-})_{x/n}\cdot mH_2O$, which consist of cationic brucite-like layers and exchangeable interlayer anions.[27–29] By virtue of this unique structure, they have been widely explored as inorganic-biology composite materials for drug/gene delivery.[30–35] Moreover, due to the electropositivity of LDHs, they tend to accelerate cellular internalization and improve cellular uptake of drugs. Doxorubicin (DOX) is an approved chemotherapeutic drug in current clinical applications, while folic acid (FA) possesses targeting capability owing to its overexpression toward cancer cells.[15,36,37] Therefore, the incorporation of DOX and FA into the interlayer gallery of LDHs would exhibit the following advantages: (i) the host–guest interactions can improve the stability and hydrophilicity of DOX, resulting in an enhancement in drug permeability/retention;[38] (ii) the intrinsic fluorescence of DOX[39] endows the composite material with the capability of fluorescence imaging. In addition, the targeting ability of FA toward cancer cells would increase the drug uptake at the cancerous site and depress cytotoxicity to normal cells.

In this work, we report a layered anti-cancer nanovehicle DOX–FA/LDH by the incorporation of DOX and FA into the LDH gallery, which shows extraordinarily good anticancer behavior, low cytotoxicity, as well as excellent targeted ability. XRD and UV-vis spectroscopy confirm that DOX and FA molecules are co-intercalated in the interlayer region of the

[a] State Key Laboratory of Chemical Resource Engineering, Beijing University of Chemical Technology, Beijing 100029, P. R. China. E-mail: liangruizheng2000@163.com, weimin@mail.buct.edu.cn; Fax: +86-10-6442-5385
[b] Beijing Shijitan Hospital Capital Medical University Beijing, 100038, P. R. China. E-mail: yd277@126.com

† Electronic supplementary information (ESI) available: XRD patterns and FT-IR spectra are displayed in Fig. S1. The SEM images and DLS results are shown in Fig. S2 and S3. Distributions of tilt angle θ_1 of DOX and θ_2 of FA with respect to hydroxide sheets in the MD simulation models are presented in Fig. S5. Fluorescence images of L02 and HepG2 incubated with DOX-FA/LDHs for 3 h and 24 h are indicated in Fig. S7. See DOI: 10.1039/c5tb02521d

LDH matrix successfully. The DOX–FA/LDH material displays a uniform nanoplatelet morphology with an average diameter of ~171 nm. *In vitro* tests performed with HepG2 cells demonstrate both fluorescence imaging and anticancer performance of DOX–FA/LDH, with a rather low cytotoxicity to the normal cells (performed with L02 cells). Moreover, the DOX–FA/LDH nanovehicle displays a high storage stability, good biocompatibility and targeting capability, which would guarantee its practical applications.

Results and discussion

Monodisperse DOX–FA/LDH was synthesized using the separate nucleation and aging steps (SNAS) method[40] reported by our group, *via* the co-intercalation of DOX and FA into the gallery of LDHs. Scheme 1 illustrates the fabrication and the cancer cell mediated endocytosis of the DOX–FA/LDH nanovehicle. In order to determine the optimal DOX loading, a series of DOX(x%)–FA(80%)/LDH composite materials were prepared and their XRD patterns are shown in Fig. 1a. For the LDH precursor, its XRD pattern reveals a series of (00l) reflections with a (003) basal spacing of 0.73 nm (2θ 12.14°), indicating a typical CO_3^{2-}–LDH (Fig. S1a, ESI†). After the co-incorporation of DOX and FA into the LDH gallery, the (003) reflection of DOX(x%)–FA(80%)/LDH composites moves from 2θ 12.14° to a lower angle (3.86°–4.82°) and the corresponding basal spacing expands from 0.73 nm to 1.83–2.28 nm (Table S1, ESI†), indicating the intercalation of FA and DOX.

The co-intercalation of FA and DOX was studied by the FT-IR spectroscopy (Fig. S1b, ESI†). Compared with the spectrum of pristine LDHs, the new band at 1611 cm^{-1} is attributed to the –C=N stretching vibration of the pterin ring in FA[41], while the bands at 1184 cm^{-1} and 1497 cm^{-1} correspond to the $\delta(CH_3O–)$ and δ(N–H) stretching vibrations of DOX, which indicates the conjugation of FA and DOX. The intensity of DOX characteristic bands (1184 and 1497 cm^{-1}) increases gradually along with the enhancement of DOX loading (from 0.5% to 3%). Furthermore, the chemical compositions of these DOX(x%)–FA(80%)/LDH composites were measured by inductively coupled plasma atomic emission spectroscopy (ICP-AES) and are listed in Table S2. SEM images (Fig. 1c and Fig. S2, ESI†) show that the DOX(x%)–FA(80%)/LDH samples display a uniform plate-like morphology. The hydrodynamic diameter (Fig. S3 and Table S3, ESI†) of these samples is also determined and the particle size gradually increases along with the enhancement of DOX loading from 0.5% to 3%. It has been reported that the clathrin-mediated endocytosis of the LDH nanovehicle is forbidden if the particle size is beyond ~300 nm.[42] Taking into account the colloidal stability and cellular uptake, the DOX(2%)–FA(80%)/LDH sample (~171 nm) was chosen for the following study. The HRTEM image of DOX(2%)–FA(80%)/LDH (Fig. 1d) shows a uniform plate-like morphology, with a lattice fringe of 0.15 nm attributed to the (110) plane of an LDH phase.

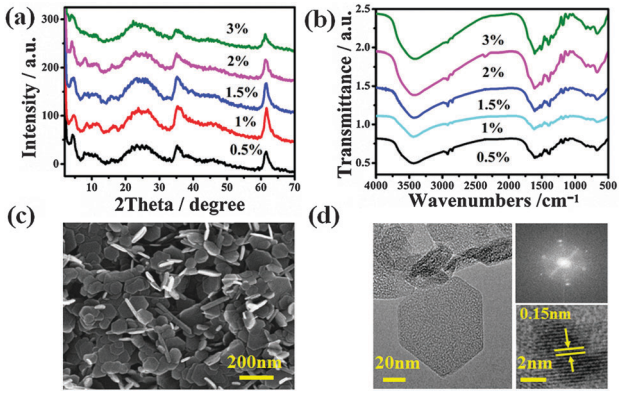

Fig. 1 (a) XRD patterns and (b) FTIR spectra of DOX(x%)–FA(80%)/LDH samples (x ranges from 0.5% to 3%). (c) SEM and (d) HRTEM images of DOX(2%)–FA(80%)/LDH; the insets in (d) display the lattice fringe and Fourier transform image.

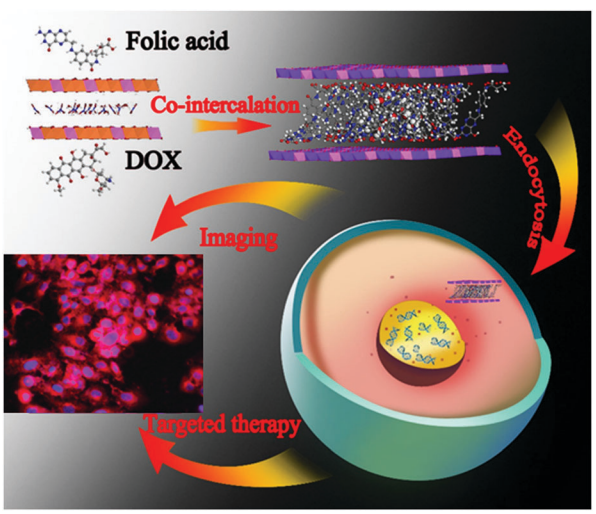

Scheme 1 Schematic illustration of the DOX–FA/LDH composite material as a nanovehicle for imaging and therapy.

The intercalated structure was further investigated using UV-vis absorption spectrometry (Fig. 2a). The pristine DOX shows a broad UV absorption with characteristic peaks at 233 nm and 488 nm. After the intercalation into the LDH gallery, an obvious red-shift is observed with the typical absorption peak at 556 nm. The red-shift can be ascribed to the collapse of the aggregation state of DOX owing to the host–guest interaction. For the DOX–FA/LDH sample, an additional peak at 285 nm is observed compared with DOX/LDH, originating from the absorption of FA. Owing to the inherent fluorescence properties of DOX, both DOX/LDH and DOX–FA/LDH are endowed with fluorescence capability, and Fig. 2b displays the photoluminescence (PL) spectra of DOX, DOX/LDH and DOX–FA/LDH with the same DOX loading. It should be noted that the fluorescence intensity of DOX/LDH and DOX–FA/LDH decreases after the intercalation relative to pristine DOX, as a result of the variation of the microenvironment. Moreover, the Zeta potential of these samples was measured in aqueous solutions. The DOX/LDH is positively-charged with a zeta potential of +21.2 mV; while DOX–FA/LDH is negatively-charged with −24.1 mV (Fig. 2c), indicating the additional loading of FA anions. For the DOX/LDH, it undergoes a passive

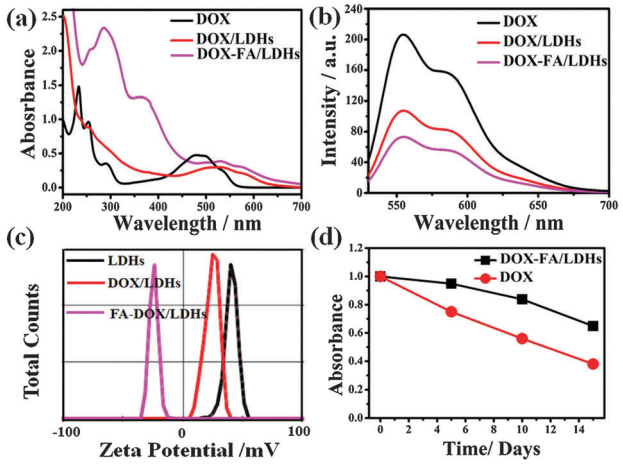

Fig. 2 (a) UV-vis absorption and (b) photoluminescence spectra of DOX, DOX/LDH and DOX–FA/LDH. (c) Zeta potentials of LDHs, DOX/LDH and DOX–FA/LDH. (d) Stability tests of DOX and DOX–FA/LDHs.

type of internalization based on the EPR effect, followed by clathrin-mediated endocytosis similar to previously reported drug–LDH hybrids.[43] The positively charged DOX/LDH nanoparticles are favorable for the uptake of cells with negatively charged cell membranes, accounting for their passive targeting ability. However, the DOX–FA/LDH nanovehicle conjugated with folic acid can be internalized inside the cells *via* folate receptor (FR)-mediated active cancer targeting followed by cell uptake.[44] Thus, the surface negative charge of the DOX–FA/LDH sample may somewhat impose an influence but cannot significantly affect its cellular uptake. In addition, the DOX–FA/LDH sample undergoes a slow and controlled release of DOX with a 69.44% release ratio within 48 h (Fig. S4, ESI†). We further investigated the stability of DOX and DOX–FA/LDH using UV-vis absorption spectroscopy (Fig. 2d) at various time points. The absorbance of pristine DOX decreases sharply from 1 day to 15 days, and a loss of 62% is found. In contrast, for the DOX–FA/LDH sample, it presents a relatively high stability at room temperature, with a slow decline of 35% after 15 days. Therefore, the intercalation of DOX and FA into the LDH gallery can improve DOX stability to a large extent, which is desirable for storage and further clinical applications.

In order to shed light on the orientation and arrangement of the co-intercalated DOX and FA in LDHs at the atomic-level, molecular dynamics (MD) simulations were performed over the DOX(2%)–FA(80%)/LDH sample. The structural model contains 96 Mg and 48 Al so as to keep the charge balance, and Fig. 3 displays the model geometry after the MD simulations. The simulated d_{003} value is 2.10 nm, in approximate agreement with the XRD data (2.28 nm). According to the simulated results, the DOX and FA molecules are slantwise oriented in the interlayer region and the tilt angles of the tail vectors (as defined in Fig. S5, ESI†) in DOX and FA with respect to the host layer are calculated to be θ_1 = 45.92° and θ_2 = 70.40°, respectively. The distance between the carboxyl group in FA and the hydroxyl group in DOX is as short as ~2.0 Å (Fig. 3b), within the interaction range of hydrogen bonding.

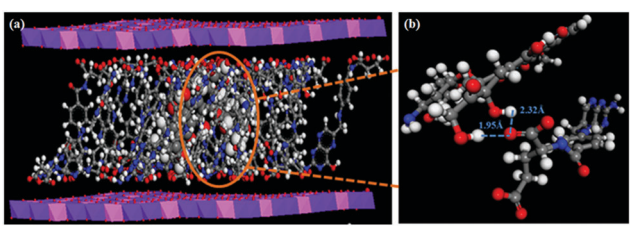

Fig. 3 The model geometry of DOX(2%)–FA(80%)/LDH after MD simulations.

The efficient internalization of cancer cells toward the drug is essential for cancer therapy, and the drug intake was firstly investigated through fluorescence imaging. HepG2 cells were used to incubate with LDH, DOX, DOX/LDH, DOX–FA/LDH samples for 24 h, and their fluorescence images were recorded. As shown in Fig. 4a–c, no fluorescence is observed when the cells are treated with pristine LDHs. For pure DOX, a weak red signal is detected (Fig. 4e), indicating the intake of DOX by HepG2 cells. As shown in Fig. 4f, the overlapped red fluorescence signal of DOX and the blue signal of DAPI can be detected, manifesting that DOX is located in the cell cytoplasm. In the case of DOX/LDH, a relatively strong fluorescence intensity is observed, indicating an effective cell uptake of the DOX/LDH (Fig. 4g–i). In addition, compared with pristine DOX and DOX/LDH, the fluorescence intensity of DOX–FA/LDH is significantly heightened with further introduction of FA (Fig. 4j–l), indicating the best intake performance owing to the targeting ability of FA toward HepG2 cells. A similar result is obtained in KB cancer cells (Fig. S6, ESI†), demonstrating the targeting uptake ability of DOX–FA/LDH.

The anticancer activity of DOX–FA/LDH was further studied by *in vitro* tests performed with HepG2 cells and normal liver L02 cells. The HepG2 cells were incubated with DOX, DOX(2%)/LDH

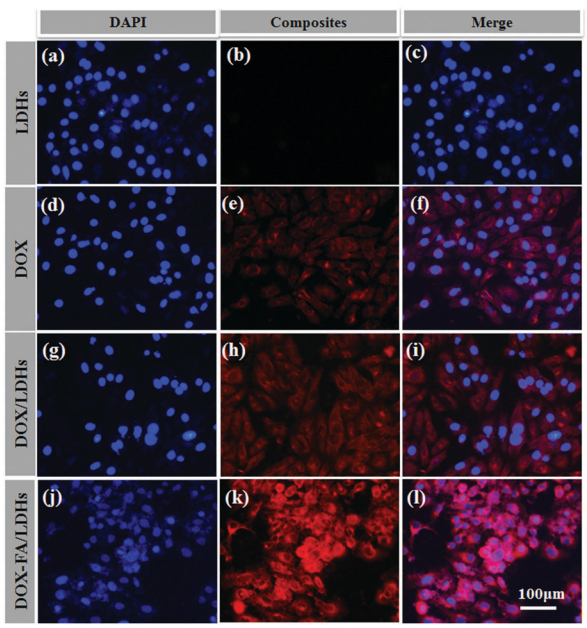

Fig. 4 Fluorescence imaging of HepG2 incubated with LDHs, DOX, DOX/LDH and DOX–FA/LDH.

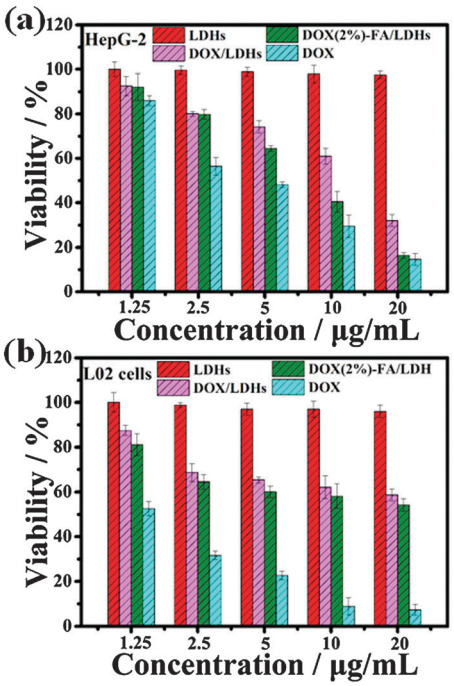

Fig. 5 Viability tests of (a) HepG2 and (b) L02 treated with LDHs, DOX/LDH, DOX(2%)–FA(80%)/LDH and DOX for 24 h.

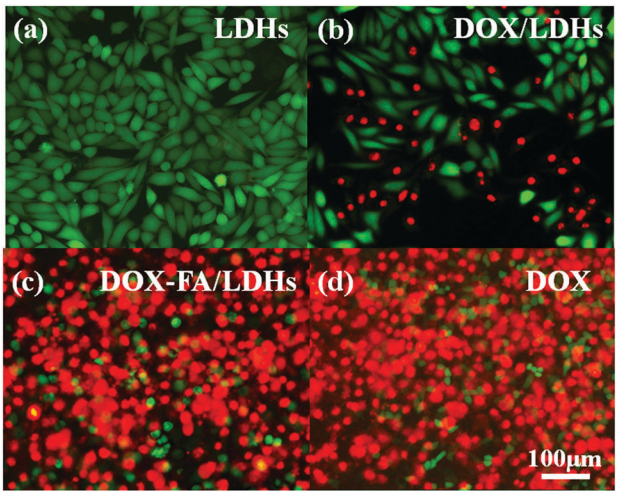

Fig. 6 Fluorescence imaging of LDHs, DOX/LDH, DOX–FA/LDH and DOX. Live and dead HepG2 cells are green and red (Calcein AM/PI), respectively.

and DOX(2%)–FA(80%)/LDH with equivalent DOX concentrations ranging from 1.25 to 20 μg mL^{-1} for 24 h, washed thoroughly with PBS, and then determined by the MTT assay. As shown in Fig. 5a, a significant anticancer effect occurs which enhances gradually along with the increase of dosage from 1.25 to 20 μg mL^{-1}. The half maximal inhibitory concentration (IC_{50}) of DOX is 4.36 μg mL^{-1}, which is less than that of DOX(2%)/LDH (19.21 μg mL^{-1}), and DOX(2%)–FA(80%)/LDH (7.14 μg mL^{-1}). This is due to the rapid uptake of DOX while both the DOX(2%)/LDH and DOX(2%)–FA(80%)/LDH undergo an uptake–delivery–release procedure. Moreover, compared with the HepG2 cells treated with DOX(2%)/LDH (IC_{50} = 19.21 μg mL^{-1}), the anticancer efficacy of DOX(2%)–FA(80%)/LDH (IC_{50} = 7.14 μg mL^{-1}) is remarkably enhanced *via* conjugation with FA, demonstrating the effectiveness of FA for specifically targeting HepG2 cells. Furthermore, we investigated the cytotoxicity of the DOX, DOX(2%)/LDH and DOX(2%)–FA(80%)/LDH with various drug concentrations toward L02 cells. Based on the MTT assay, the viability reveals that L02 cells show a strong tolerance to DOX(2%)–FA(80%)/LDH with an IC_{50} as high as 22.81 μg mL^{-1}, which is 3.19 times larger than that of HepG2 cells (7.14 μg mL^{-1}). In contrast, pristine DOX displays a much stronger cytotoxicity toward L02 cells (IC_{50} = 1.31 μg mL^{-1}) than HepG2 cells (IC_{50} = 4.36 μg mL^{-1}). Therefore, the DOX(2%)–FA(80%)/LDH sample exhibits an enhanced biocompatibility compared with pristine DOX.

In order to make a comparison of DOX, DOX(2%)/LDH and DOX(2%)–FA(80%)/LDH, specific anticancer efficacy (SAE) is denoted as the difference value of viability between L02 and HepG2 cells. The DOX(2%)–FA(80%)/LDH drug exhibits a rather large SAE(17.71%), superior to that of the DOX(2%)/LDH(−1.15%) and DOX(−20.71%) with an equivalent DOX concentration of 10 μg mL^{-1}. The results verify that DOX(2%)–FA(80%)/LDH plays a positive role in anticancer activity, while pristine DOX shows an obvious side-effect. We further investigated the reason for different viabilities of HepG2 and L02 cells toward DOX(2%)–FA(80%)/LDH, by monitoring the cell uptake of drug at different time points. As shown in Fig. S7 (ESI†), the fluorescence intensity of HepG2 cells is much stronger than that of L02 cells after 3 h incubation, indicating the fast internalization of HepG2 cells toward DOX(2%)–FA(80%)/LDH. Moreover, DOX(2%)–FA(80%)/LDH shows a time-dependent internalization behavior for HepG2 cells, and the accumulation maximum is observed after 24 h. In contrast, the fluorescence intensity of L02 cells decreases significantly after 24 h incubation. The above results demonstrate that the overexpression of the FA receptor toward HepG2 cells promotes the uptake of DOX(2%)–FA(80%)/LDH, accounting for its excellent anticancer effectiveness.

To visualize the anticancer effect of the drug, the dead and live HepG2 cells were stained with propidium iodide (PI) and Calcein-AM, respectively. The fluorescence microscopy image shows that HepG2 cells treated with the pristine LDH sample (Fig. 6a) display no obvious apoptosis after 24 h incubation. The addition of DOX/LDH (10 μg mL^{-1}) causes partial apoptosis (Fig. 6b), indicating a weak anticancer performance. In contrast, the HepG2 cells treated with DOX(2%)–FA(80%)/LDH (10 μg mL^{-1}) exhibit an intense PI signal (Fig. 6c), demonstrating a predominant apoptosis after 24 h incubation. HepG2 cells treated with DOX (10 μg mL^{-1}) also display a similar PI signal (Fig. 6d). Although DOX(2%)–FA(80%)/LDH and DOX exhibit close anticancer effectiveness, the former shows a weak cytotoxicity and largely enhanced biocompatibility, as a result of the incorporation of the LDH nanovehicle.

Conclusions

In summary, a supermolecular nanovehicle based on the intercalation of FA and DOX into the LDH gallery was successfully

fabricated. DOX–FA/LDH shows a platelet-like morphology with a particle size of ~171 nm. *In vitro* experiments show that DOX–FA/LDH exhibits good imaging properties and obviously increased targeting uptake. Moreover, the DOX–FA/LDH nanovehicle produces a strong suppression on the proliferation of HepG2 cells while a highly decreased toxicity to the normal L02 cells as a result of the over-expression of FA toward HepG2 cells. The enhanced biocompatibility would guarantee its application in cancer imaging and therapy.

Experimental

Reagents and materials

DOX and FA were purchased from Sigma-Aldrich Company. Analytical grade chemicals including $Mg(NO_3)_2{\cdot}6H_2O$, $Al(NO_3)_3{\cdot}9H_2O$, NaOH, acetone and ethanol were purchased from Aladdin company and used without further purification. DMEM (Dulbecco's modified Eagle's medium), FBS (Fetal bovin serum), PBS (Phosphate buffer solution) were purchased from Beijing Solarbio Science and Technology Company. Deionized water was utilized throughout the whole experimental process.

Synthesis of the composite

The DOX–FA/LDH composite was prepared according to the SNAS method reported by our group previously.[40] Typically, 40 mL of solution A ($Mg(NO_3)_2{\cdot}6H_2O$: 0.003 mol, $Al(NO_3)_3{\cdot}9H_2O$: 0.0015 mol and DOX: 3.0×10^{-5} mol) and 40 mL of solution B (NaOH: 0.01 mol and FA: 0.0012 mol) were simultaneously added to a colloid mill with a rotor speed of 3000 rpm and mixed for 1 min. The colloid suspension was transferred into a Teflon-lined stainless steel autoclave. After hydrothermal treatment at 100 °C for 24 h, the product was centrifuged 3 times with deionized water and ethanol followed by drying in an oven at 60 °C overnight.

Fluorescence imaging studies of the composites

HepG2 cells were grown and expanded in Dulbecco's modified Eagle's medium (DMEM) supplemented with 10% fetal bovine serum (FBS) and 1% penicillin–streptomycin at 37 °C under a 5% CO_2 atmosphere. After reaching 80–90% confluence, the HepG2 cells were washed with PBS and afterwards detached from the flask by addition of 1.0 mL of 0.25% trypsin for 1–3 min at 37 °C. To study the cellular uptake of DOX, DOX/LDH and DOX(2%)–FA(80%)/LDH, HepG2 cells (1×10^4 cells per well) were firstly seeded in a 96-well plate and cultured in a humid 5% CO_2 atmosphere for 24 h at 37 °C. Then, pristine DOX, DOX/LDH and DOX(2%)–FA(80%)/LDH (equivalent DOX: 10 μg mL^{-1}) were added into the wells and further incubated for 24 h. Subsequently, the cells were washed three times with PBS followed by stained with 3 mg mL^{-1} DAPI for 20 min and further washing with PBS. Finally, a fluorescence microscope was used to determine the drug uptake through the fluorescence intensity of DOX.

In vitro cell assay

To study the integrated performance of DOX, DOX/LDH and DOX(2%)–FA(80%)/LDH, HepG2 cells and L02 cells were used to evaluate their anti-cancer activity and cytotoxicity, respectively. Specifically, HepG2 cells and L02 cells (1×10^4 cells per well) were seeded into two 96-well plates. After incubation of 24 h, pristine DOX, DOX/LDH and DOX(2%)–FA(80%)/LDH with concentrations in the range 1.25–20 μg mL^{-1} were added into the wells and further incubated for 24 h. After washing three times with PBS, colorimetric 3-(4,5-dimethylthiazol-2-yl)-2,5-diphenyltetrazolium bromide (MTT) was used to determine the cell viability.

Sample characterization

Powder X-ray diffraction (XRD) patterns were recorded using a Rigaku XRD-6000 diffractometer, using Cu Kα radiation (λ = 0.15418 nm) at 40 kV, 30 mA, with a step of 0.04°/2θ in the range from 3 to 70°. UV-vis absorption spectra were collected in the range 200–700 nm on a Shimadzu U-3000 spectrophotometer, with a slit width of 1.0 nm. The photoluminescence spectra were tested on a RF-5301PC fluorospectrophotometer with an excitation wavelength at 490 nm. The zeta potential and dynamic lighting scatting (DLS) diameter were measured by photon correlation spectroscopy (PCS, Nanosizer Nano ZS, MALVERN Instruments). The chemical compositions were measured by inductively coupled plasma (ICP) emission spectroscopy (Shimadzu ICPS-7500). The morphology of composites was investigated using a scanning electron microscope (SEM; Zeiss SUPRA 55) with an accelerating voltage of 20 kV. Transmission electron microscopy (TEM) images were recorded using a JEOL JEM-2100 high resolution transmission electron microscope with an accelerating voltage of 200 kV. The Fourier transform infrared spectra (FT-IR) were obtained using a Vector 22 (Bruker) spectrophotometer using the KBr pellet technique in the range 4000–400 cm^{-1} with 2 cm^{-1} resolution. The fluorescence imaging photograph was obtained using a Nikon Ti-S fluorescence microscope with a 40-fold enlargement.

Acknowledgements

This work was supported by the 973 Program (Grant No. 2014CB932103), the National Natural Science Foundation of China (NSFC), the Innovation and Promotion Project of Beijing University of Chemical Technology and the Fundamental Research Funds for the Central Universities (YS 1406).

Notes and references

1 J. Zhang, Y.-C. Liang, X. Lin, X. Zhu, L. Yan, S. Li, X. Yang, G. Zhu, A. L. Rogach and P. K. Yu, *ACS Nano*, 2015, **9**, 9741–9756.
2 Z. Zhang, J. Wang and C. Chen, *Adv. Mater.*, 2013, **25**, 3869–3880.
3 R. Liang, R. Tian, L. Ma, L. Zhang, Y. Hu, J. Wang, M. Wei, D. Yan, D. G. Evans and X. Duan, *Adv. Funct. Mater.*, 2014, **24**, 3144–3151.
4 Y. Wang, W. Li, Y. Yang, Q. Zeng, K.-H. Wong, X. Li and T. Chen, *J. Mater. Chem. B*, 2015, **3**, 9374–9382.
5 W.-W. Qi, H.-Y. Yu, H. Guo, J. Lou, Z.-M. Wang, P. Liu, A. Sapin-Minet, P. Maincent, X.-C. Hong, X.-M. Hu and Y.-L. Xiao, *Mol. Pharmaceutics*, 2015, **12**, 675–683.

6 L. Chen, Y. Xue, X. Xia, M. Song, J. Huang, H. Zhang, B. Yu, S. Long, Y. Liu, L. Liu, S. Huang and F. Yu, *J. Mater. Chem. B*, 2015, **3**, 8949–8962.
7 K. Li, Q. Su, W. Yuan, B. Tian, B. Shen, Y. Li, W. Feng and F. Li, *ACS Appl. Mater. Interfaces*, 2015, **7**, 12278–12286.
8 J. Li, Y. Hu, J. Yang, P. Wei, W. Sun, M. Shen, G. Zhang and X. Shi, *Biomaterials*, 2015, **38**, 10–21.
9 J. Zeng, L. Jing, Y. Hou, M. Jiao, R. Qiao, Q. Jia, C. Liu, F. Fang, H. Lei and M. Gao, *Adv. Mater.*, 2014, **26**, 2694–2698.
10 Y. Wang and H. Gu, *Adv. Mater.*, 2015, **27**, 576–585.
11 Y. Liu, J. Bai, X. Jia, X. Jiang and Z. Guo, *ACS Appl. Mater. Interfaces*, 2015, **7**, 112–121.
12 T. Chen, S. Xu, T. Zhao, L. Zhu, D. Wei, Y. Li, H. Zhang and C. Zhao, *ACS Appl. Mater. Interfaces*, 2012, **4**, 5766–5774.
13 P. L. Truong, X. Ma and S. J. Sim, *Nanoscale*, 2014, **6**, 2307–2315.
14 H. Wang, L. Zheng, C. Peng, M. Shen, X. Shi and G. Zhang, *Biomaterials*, 2013, **34**, 470–480.
15 H.-X. Xia, X.-Q. Yang, J.-T. Song, J. Chen, M.-Z. Zhang, D.-M. Yan, L. Zhang, M.-Y. Qin, L.-Y. Bai, Y.-D. Zhao and Z.-Y. Ma, *J. Mater. Chem. B*, 2014, **2**, 1945–1953.
16 J. Yang, M. H. Yao, M. S. Du, R. M. Jin, D. H. Zhao, J. Ma, Z. Y. Ma, Y. D. Zhao and B. Liu, *Chem. Commun.*, 2015, **51**, 2569–2572.
17 J. Cui, Y. Yan, Y. Wang and F. Caruso, *Adv. Funct. Mater.*, 2012, **22**, 4718–4723.
18 R. Dorresteijn, N. Billecke, M. Schwendy, S. Pütz, M. Bonn, S. H. Parekh, M. Klapper and K. Müllen, *Adv. Funct. Mater.*, 2014, **24**, 4026–4033.
19 F. Li, X. Zhao, H. Wang, R. Zhao, T. Ji, H. Ren, G. J. Anderson, G. Nie and J. Hao, *Adv. Funct. Mater.*, 2015, **25**, 788–798.
20 H. Deng, X. Zhao, J. Liu, L. Deng, J. Zhang, J. Liu and A. Dong, *J. Mater. Chem. B*, 2015, **3**, 9397–9408.
21 X. Hu, J. Hu, J. Tian, Z. Ge, G. Zhang, K. Luo and S. Liu, *J. Am. Chem. Soc.*, 2013, **135**, 17617–17629.
22 P. Huang, D. Wang, Y. Su, W. Huang, Y. Zhou, D. Cui, X. Zhu and D. Yan, *J. Am. Chem. Soc.*, 2014, **136**, 11748–11756.
23 C. Y. Sun, Y. C. Ma, Z. Y. Cao, D. D. Li, F. Fan, J. X. Wang, W. Tao and X. Z. Yang, *ACS Appl. Mater. Interfaces*, 2014, **6**, 22709–22718.
24 M. H. Xiong, Y. Bao, X. Z. Yang, Y. C. Wang, B. Sun and J. Wang, *J. Am. Chem. Soc.*, 2012, **134**, 4355–4362.
25 J. Yu, C. Yang, J. Li, Y. Ding, L. Zhang, M. Z. Yousaf, J. Lin, R. Pang, L. Wei, L. Xu, F. Sheng, C. Li, G. Li, L. Zhao and Y. Hou, *Adv. Mater.*, 2014, **26**, 4114–4120.
26 H. Wang, C. A. Thorling, X. Liang, K. R. Bridle, J. E. Grice, Y. Zhu, D. H. G. Crawford, Z. P. Xu, X. Liu and M. S. Roberts, *J. Mater. Chem. B*, 2015, **3**, 939–958.
27 J. R. Rees, C. S. Burden and A. M. Fogg, *J. Solid State Chem.*, 2015, **224**, 36–39.
28 L. N. Ribeiro, A. C. Alcantara, M. Darder, P. Aranda, F. M. Araujo-Moreira and E. Ruiz-Hitzky, *Int. J. Pharm.*, 2014, **463**, 1–9.
29 D.-H. Park, G. Choi and J.-H. Choy, *Struct. Bonding*, 2015, **166**, 137–175.
30 J.-H. Choy, S.-Y. Kwak, Y.-J. Jeong and J.-S. Park, *Angew. Chem., Int. Ed.*, 2000, **39**, 4041–4045.
31 D.-H. Park, J.-E. Kim, J.-M. Oh, Y.-G. Shul and J.-H. Choy, *J. Am. Chem. Soc.*, 2010, **132**, 16735–16736.
32 Q. Wang and D. O'Hare, *Chem. Rev.*, 2012, **112**, 4124–4155.
33 K. Khorsandi, R. Hosseinzadeh and M. Fateh, *RSC Adv.*, 2015, **5**, 93987–93994.
34 L. Yan, W. Chen, X. Zhu, L. Huang, Z. Wang, G. Zhu, V. A. L. Roy, K. N. Yu and X. Chen, *Chem. Commun.*, 2013, **49**, 10938–10940.
35 S.-J. Choi, J.-M. Oh, H.-E. Chung, S.-H. Hong, I.-H. Kim and J.-H. Choy, *Curr. Pharm. Des.*, 2013, **19**, 7196–7202.
36 J. M. Shen, X. M. Guan, X. Y. Liu, J. F. Lan, T. Cheng and H. X. Zhang, *Bioconjugate Chem.*, 2012, **23**, 1010–1021.
37 Y.-S. Yoon, B.-I. Lee, K. S. Lee, G. H. Im, S.-H. Byeon, J. H. Lee and I. S. Lee, *Adv. Funct. Mater.*, 2009, **19**, 3375–3380.
38 L. Wang, H. Xing, S. Zhang, Q. Ren, L. Pan, K. Zhang, W. Bu, X. Zheng, L. Zhou, W. Peng, Y. Hua and J. Shi, *Biomaterials*, 2013, **34**, 3390–3401.
39 C. Yu, M. Zhou, X. Zhang, W. Wei, X. Chen and X. Zhang, *Nanoscale*, 2015, **7**, 5683–5690.
40 Y. Zhao, F. Li, R. Zhang, D. G. Evans and X. Duan, *Chem. Mater.*, 2002, **14**, 4286–4291.
41 S. Cui, D. Yin, Y. Chen, Y. Di, H. Chen, Y. Ma, S. Achilefu and Y. Gu, *ACS Nano*, 2012, **7**, 676–688.
42 J.-M. Oh, S.-J. Choi, G.-E. Lee, J.-E. Kim and J.-H. Choy, *Chem. – Asian J.*, 2009, **4**, 67–73.
43 J.-M. Oh, S.-J. Choi, S.-T. Kim and J.-H. Choy, *Bioconjugate Chem.*, 2006, **17**, 1411–1417.
44 J.-M. Oh, S.-J. Choi, G.-E. Lee, S.-H. Han and J.-H. Choy, *Adv. Funct. Mater.*, 2009, **19**, 1617–1624.

